JMEPEG (2012) 21:1300–1308
DOI: 10.1007/s11665-011-0035-9

1059-9495/$19.00

# Corrosion Behavior of Magnesium Alloy AP65 in 3.5% Sodium Chloride Solution

*Nai-guang Wang, Ri-chu Wang, Chao-qun Peng, and Yan Feng*

*(Submitted April 30, 2011; in revised form August 2, 2011)*

**Magnesium alloy AP65 was prepared by melting and casting. The corrosion behavior of the as-cast and solid solution (T4)-treated AP65 alloys in 3.5% sodium chloride solution was investigated by corrosion morphology observation, immersion test, and electrochemical measurements. The results show that the second phase $Mg_{17}Al_{12}$ surrounded by a lead-enriched area distributes discontinuously along the grain boundaries in the as-cast AP65 alloy. The lead-enriched areas with high activity are susceptible to be attacked during immersion test and can act as places for preferential anodic dissolution. The corrosion resistance of the as-cast AP65 alloy can be improved after T4 treatment and the T4-treated alloy suffers general corrosion.**

**Keywords** AP65 alloy, corrosion resistance, electrochemical measurement, hydrogen evolution, mass loss rate

## 1. Introduction

Because of the rapid activation, high cell voltage, wide voltage range, high power density capability, relatively low density, low electrode potential and long un-activated storage life (Ref 1-3), magnesium alloys have been developed as anode materials used in seawater battery system and cathodic protection such as in sonobuoys, beacons, emergency equipments, balloon batteries, and life jackets (Ref 4, 5). However, a critical limitation for the service of magnesium anode is their susceptibility to corrosion (Ref 6, 7).

The corrosion of magnesium anode is mainly controlled by the composition of the α-Mg matrix, the volume fraction of the second phase and the electrochemical property of the second phase (Ref 8). AP65 is one of these magnesium anodes with a nominal composition of Mg-6%Al-5%Pb (mass fraction). It is reported that aluminum, added into the magnesium matrix, can enhance the corrosion resistance of magnesium alloys in sodium chloride solution (Ref 8-11). It has also been demonstrated that the corrosion resistance of magnesium alloys can be improved with a small quantity of lead in the magnesium matrix (Ref 12, 13). Udhayan and Bhatt (Ref 14) studied the corrosion behavior of AP65 in various concentrations of magnesium perchlorate solutions and found that its electrode/electrolyte interfacial process is determined by an activation-controlled reaction. However, so far, there are few reports about the corrosion behavior of AP65 alloy under different conditions in sodium chloride solution and its corrosion mechanism is not clearly understood. The aim of this work is to study the corrosion behavior of the as-cast and T4-treated AP65 alloys and summarize their corrosion mechanisms in sodium chloride solution.

Foundation item: National key science and technological project (JPPT-115-168).

**Nai-guang Wang, Ri-chu Wang, Chao-qun Peng,** and **Yan Feng**, School of Materials Science and Engineering, Central South University, Changsha 410083, China. Contact e-mails: wangnaiguang505@163.com and wrc@mail.csu.edu.cn.

## 2. Experimental Procedures

Magnesium alloy AP65 with a nominal composition of Mg-6%Al-5%Pb-1%Zn (all compositions used in this paper are mass fractions, %) was prepared by melting together the required quantities of commercially pure magnesium (99.99%), pure aluminum (99.99%), pure lead (99.99%), and pure zinc (99.99%). Magnesium melting was carried out in a graphite crucible in the induction furnace at 730 °C with the protection of argon. The alloying elements were added 5 min before casting to avoid loss of lead due to vaporization. The molten metal was then poured into a preheated (200 °C) rectangular steel mold with a dimension of 240 × 210 × 40 mm. Sulfur dusting was done during pouring to avoid burning and reduce oxidation. The chemical composition determined by the atomic absorption spectrometry is listed in Table 1. Solution treatment (T4) of the alloy was carried out at 400 °C for 24 h in argon atmosphere followed by water quench. The as-cast and T4-treated alloys were successively ground to 1200 grit by SiC paper, finely polished using 0.5 μm diamond paste, ultrasonically cleaned in acetone and dried in cold air. For metallographic characterization, alloys were etched with 1% nital solution (nitric acid in ethanol) to reveal the second phases of the as-cast alloy and the grain boundaries of the T4-treated alloy. The microstructures of the alloys were observed by a Quanta-200 SEM using back-scattered electron (BSE) imaging. The phase structures were determined by a D/Max 2550 x-ray diffraction (XRD) with Cu $K_\alpha$ radiation. The scan range of 2θ was from 10° to 80° with a scan step of 1.2°. The elemental distribution in the second phase and magnesium matrix in the as-cast alloy was analyzed by line scan of energy dispersive x-ray spectroscopy (EDX).

The corrosion behavior of the AP65 alloy was investigated by immersion test and corrosion morphology observation. Each

**Table 1 Chemical composition of AP65 alloy (mass fraction %)**

| Alloy | Al | Pb | Zn | Si | Mn | Fe | Mg |
|---|---|---|---|---|---|---|---|
| AP65 | 5.72 | 5.27 | 0.85 | 0.04 | 0.01 | 0.03 | Bal |

alloy was encapsulated in epoxy resin with a surface of $10 \times 10$ mm exposed to 500 mL 3.5% sodium chloride solution in a beaker at 25 °C. The epoxy used here is inert to sodium chloride solution and the mass loss of it cannot occur during immersion test. Besides, there was no space between the epoxy and coupon and thus the crevice corrosion can be prevented. The electrolyte solution was made with analytical grade reagents and de-ionized water. Before each test, the alloy was ground successively to 1200 grit SiC paper and then weighed. The alloy in the beaker was covered with a funnel, over which a buret prefilled with sodium chloride solution was vertically mounted. The hydrogen bubbles evolving from the alloy surface in the course of immersion were led by the funnel into the buret and gradually displaced the test solution in the buret. In this way, the kinetics of the hydrogen evolution can be easily determined by reading the height of the test solution level in the buret. The corrosion products after immersion tests for various periods were removed by chromic acid solution with minimal dissolution of base alloy and the corroded surface morphology was observed by a Quanta-200 SEM using secondary electron (SE) imaging and BSE imaging. After the corrosion products were cleaned, the alloy was weighed again to determine the mass loss rate ($mg/cm^2/h$) caused by corrosion during immersion test.

The corrosion behavior was also studied by electrochemical measurements using an IM6ex potentiostat with a standard three-electrode glass cell. Each alloy for the measurement was encapsulated in epoxy resin with a surface of $10 \times 10$ mm exposed to 3.5% sodium chloride solution. The alloy surface was ground successively to 1200 grit SiC paper. A platinum gauze was used as the counter electrode and a saturated calomel electrode (SCE) as the reference electrode. All potentials were referred to the SCE. AC impedance measurement was conducted at the open circuit potential of the alloy after it was immersed in sodium chloride solution for 2 min. AC potential signal with an amplitude of 5 mV was applied, starting from a high frequency of 100,000 Hz to a low frequency of 0.05 Hz. The potentiodynamic polarization curve measurement was started by stepping the potential several hundred millivolts negative to the open circuit potential and then polarizing in an anodic direction. In order to reach the steady state, a scan rate of 0.5 mV/s was used and each alloy was immersed in sodium chloride solution for 2 min before potentiodynamic polarization curve measurement. All these immersion tests and electrochemical measurements were performed in triplicate to ascertain reproducibility.

## 3. Results and Discussion

### 3.1 Microstructures of AP65 Alloy

Figure 1(a) shows the BSE image of the as-cast AP65 alloy. It can be seen that the microstructure consists of primary α-Mg grains plus a second phase distributing discontinuously along the grain boundaries. The second phases are surrounded by bright areas. According to the XRD pattern shown in Fig. 2, the second phase in the as-cast AP65 alloy is $Mg_{17}Al_{12}$ (the β-phase). The elemental distribution across the second phase and α-Mg matrix was analyzed by EDX line scan as shown in Fig. 1(c). The direction of line scan is marked with the white arrow in Fig. 1(a), traversing the bright area, second phase, bright area and dark area. According to the EDX result, the bright areas surrounding the second phases are lead-enriched areas. Addition of lead has not led to the formation of any compound either with magnesium or aluminum in AP65 alloy due to the high solubility of lead in magnesium. Therefore, lead is expected to be in the solid solution, which is consistent with Ref. 12 and 15. The second phase consists of magnesium, aluminum, and zinc. Aluminum mainly distributes in the second phase. The dark areas mainly contain magnesium while the contents of the alloying elements are lower than those of the other areas. It is obvious that the elemental distribution in the as-cast alloy is not uniform, which is consistent with the observation of BSE image. Figure 1(b) shows the BSE image of the T4-treated AP65 alloy. The second phases dissolve into the α-Mg matrix and the bright and dark areas also disappear after the T4 treatment. This means that the alloying elements distribute homogeneously in the T4-treated alloy. The XRD pattern shown in Fig. 2 implies that only α-Mg phase exists in the T4-treated alloy.

### 3.2 Corrosion Morphologies of AP65 Alloy

The corrosion processes of the as-cast and T4-treated AP65 alloys were investigated using immersion test in 3.5% sodium chloride solution. Figure 3(a) shows the SE corrosion morphology of the as-cast alloy after 1 h immersion. It can be seen that the as-cast alloy suffers microgalvanic corrosion between the second phase and the surrounding lead-enriched area. The corrosion spots caused by microgalvanic corrosion mainly present in the vicinity of the second phases. The second phase keeps intact on the corroded surface due to its more positive free corrosion potential (Ref 16). Besides, many round-shaped pores caused by corrosion are also observed in the as-cast alloy as marked with arrows in Fig. 3(a). According to the corresponding BSE image shown in Fig. 3(b), these pores mainly distribute in the bright areas with high content of lead while the α-Mg matrix with less contents of alloying elements suffers less attack. Therefore, it can be concluded that the lead-enriched area in the as-cast alloy is more susceptible to be attacked during immersion test. These results prove that the second phases act as cathodes and the lead-enriched areas surrounding the second phases act as anodes during corrosion process. According to Candan et al. (Ref 12), the corrosion resistance of magnesium alloy AZ91 can be improved by adding 1% lead, attributed to a decrease of the intermetallics and an increase of aluminum content in α-Mg matrix caused by lead addition. However, in this study, the content of lead in the lead-enriched area of the as-cast AP65 alloy is as high as 6% (see Fig. 1c). Because of the high content of lead in the solid solution, the lead-enriched area with high activity is more susceptible to be attacked than the α-Mg matrix with less content of lead (see Fig. 3b). This is not consistent with the corrosion behavior of magnesium-lead binary alloys reported by Petrova and Krasnoyarakii (Ref 17). Figure 3(c) shows the SE corrosion morphology of the T4-treated alloy after 1 h immersion. It can be seen that the T4-treated alloy suffers general corrosion,

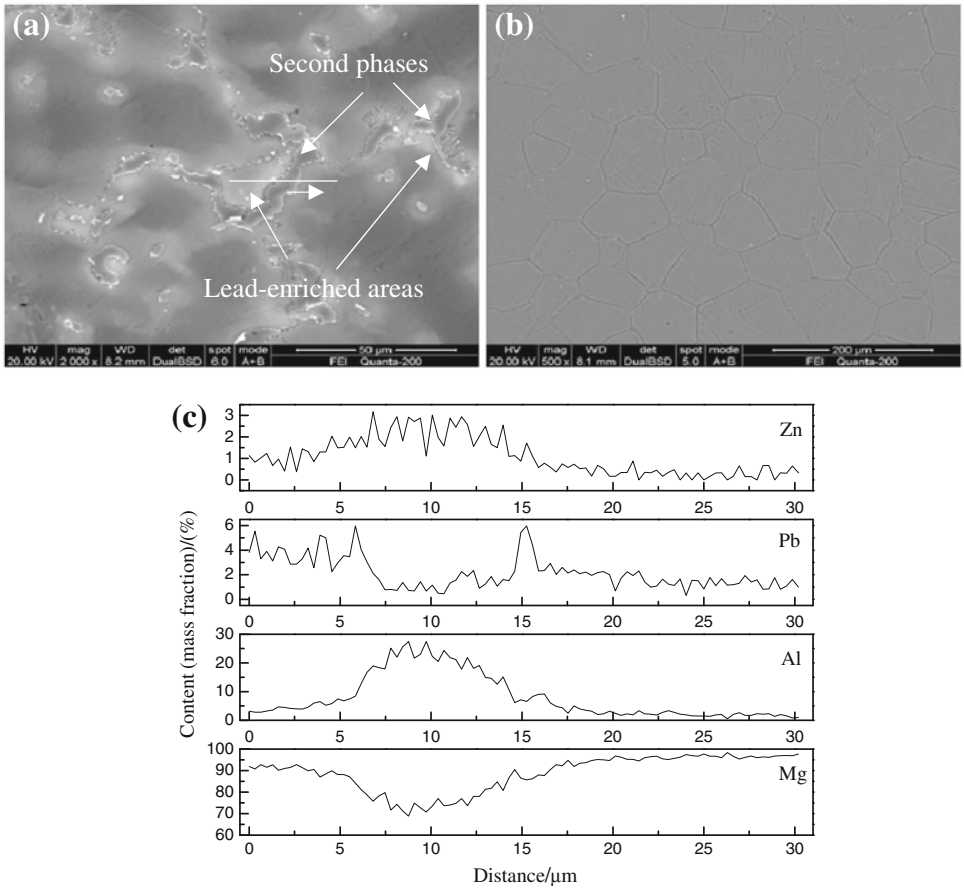


**Fig. 1** BSE (backscattered electron) images and EDX results of AP65 alloys: (a) as-cast alloy, (b) T4-treated alloy, and (c) chemical composition analysis by line scan of EDX of as-cast alloy

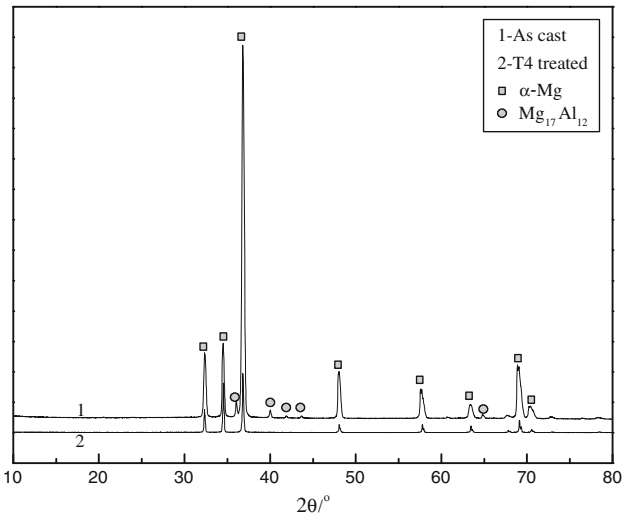


**Fig. 2** XRD patterns of AP65 alloys

initiating in the form of round-shaped pores distributing homogeneously within the grains and along the grain boundaries. This can be ascribed to the homogeneously distributing alloying elements in the T4-treated alloy. No microgalvanic accelerating effect or lead-enriched area exists in the T4-treated alloy and thus it suffers general corrosion during immersion test.

After the AP65 alloys were immersed in sodium chloride solution for 12 h, the as-cast alloy suffered more severely attack than the T4-treated one, which can be verified by the low magnification SE corrosion morphologies shown in Fig. 4. According to Fig. 4, the severely corroded area of the T4-treated alloy (Fig. 4a) is smaller than that of the as-cast one (Fig. 4b) and almost the whole surface of the as-cast alloy is attacked after 12 h immersion. Figure 4(c) shows the high magnification SE corrosion morphology of the as-cast alloy after 12 h immersion. Many second phases are still embedded in the α-Mg matrix and the corrosion spots are deeper than those of the alloy after 1 h immersion (Fig. 3a). According to the XRD pattern shown in Fig. 2, the second phase in the as-cast alloy is $Mg_{17}Al_{12}$. It serves mainly as a galvanic cathode and accelerates the corrosion of the α-Mg matrix if it presents as a small fraction while it may act mainly as an anodic barrier against the overall corrosion of the alloy if its fraction is high (Ref 16). According to Srinivasan et al. (Ref 15), the formation of $Mg_{17}Al_{12}$ distributing along the grain boundaries of the as-cast AZ91 alloy during the solidification process can be suppressed with the addition of 2% lead. In this study, the nominal composition of lead in AP65 alloy is 5% and thus the suppression effect should be larger and the size of second phase $Mg_{17}Al_{12}$ should be smaller than those of AZ91 alloy. With small size and low fraction, the anodic barrier effect of the second phase $Mg_{17}Al_{12}$ to the α-Mg matrix can be reduced. According to Fig. 1(c), zinc mainly distributes in the second phase. With high free corrosion potential, zinc distributing in

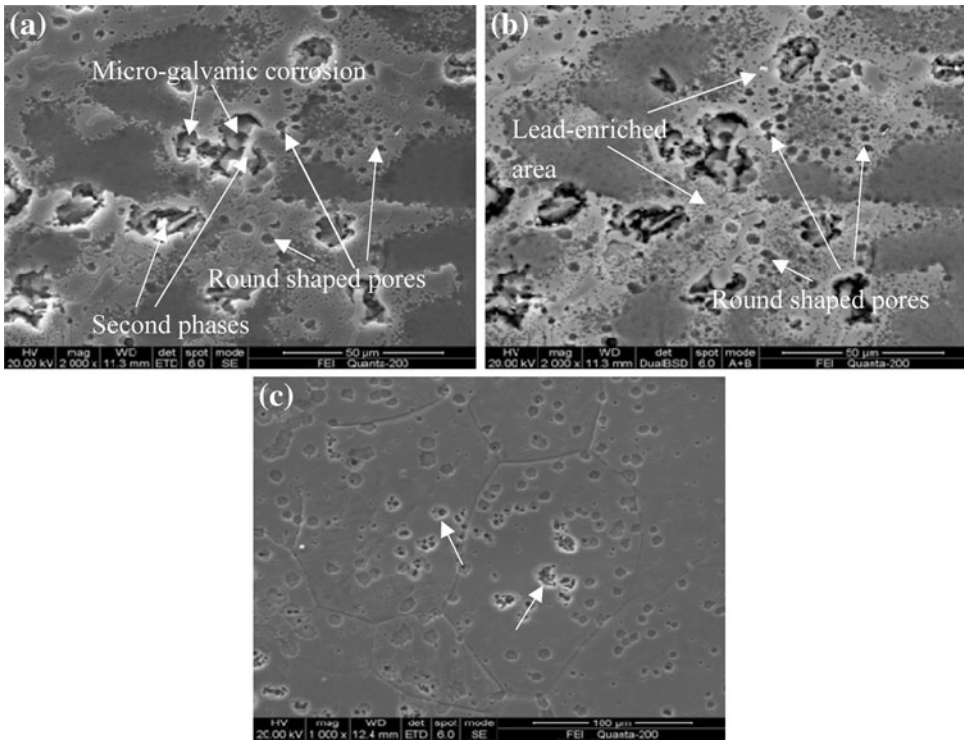


**Fig. 3** Corrosion morphologies of AP65 alloys immersed in sodium chloride solution for 1 h: (a) SE (secondary electron) image of as-cast alloy, (b) BSE (backscattered electron) image of as-cast alloy, and (c) SE (secondary electron) image of T4-treated alloy

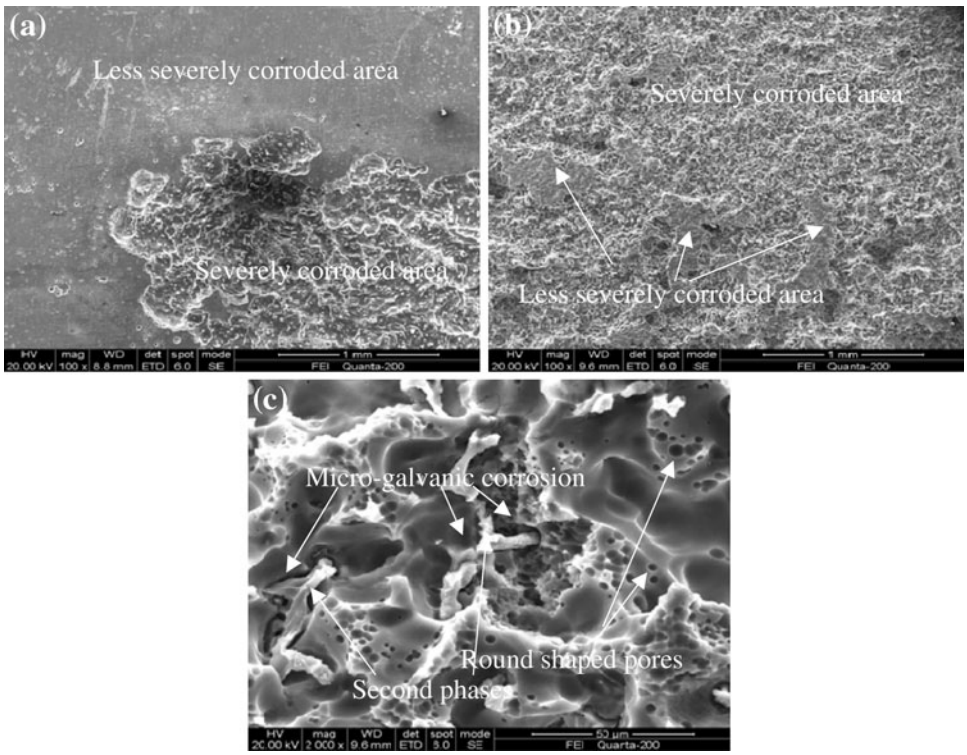


**Fig. 4** SE (secondary electron) corrosion morphologies of AP65 alloys immersed in sodium chloride solution for 12 h: (a) low magnification morphology of T4-treated alloy, (b) low magnification morphology of as-cast alloy, and (c) high magnification morphology of as-cast alloy

the second phase makes the free corrosion potential of the second phase much more positive than that of the α-Mg matrix. Therefore, the microgalvanic corrosion between the second phase and the α-Mg matrix can be accelerated. Besides, the round-shaped pores distributing on the lead-enriched area after 12 h immersion are also deeper than those of the alloy after 1 h

immersion (Fig. 3a). This means for the as-cast alloy, the corrosion aggravates as the immersion time increases, leading to the larger severely corroded area of the as-cast alloy compared with that of the T4-treated one.

With the increase of immersion time up to 60 h, the round-shaped pores distributing on the lead-enriched area in the as-cast alloy are difficult to be identified and some second phases are still embedded in the α-Mg matrix while others are peeled off from the matrix, leaving some round pits on the corroded surface as marked with arrows in Fig. 5(a). According to Fig. 1(a), in the as-cast alloy the second phases are surrounded by the lead-enriched areas, which are more susceptible to corrosion than other areas (Fig. 3b). Besides, the microgalvanic corrosion between the α-Mg matrix and the second phase also makes the lead-enriched area attacked. Therefore, the anodic dissolution of the lead-enriched area will be accelerated, leading to the peeling off of the second phases and the disappearance of the round-shaped pores distributing on the lead-enriched areas. After 60 h immersion, there are still some second phases embedded in the α-Mg matrix as marked with arrows in Fig. 5(a). They can continue to accelerate the corrosion of the α-Mg matrix with the increase of immersion time. Figure 5(b) shows the SE corrosion morphology of the T4-treated alloy after 60 h immersion. There are still many round-shaped pores distributing homogeneously within the grain and along the grain boundaries, which can be ascribed to the homogeneously distributing alloying elements in the T4-treated alloy. Compared with those of the T4-treated alloy immersed for 1 h, these pores become deeper after 60 h immersion. As the immersion time increases, the corrosion of the T4-treated alloy spreads to the whole surface of the alloy and the corrosion develops downward, which still initiates in the form of general corrosion and the round pores caused by corrosion distribute homogeneously within the grain and along the grain boundaries.

### 3.3 Mass Loss Rates and Hydrogen Evolution Volumes of AP65 Alloy

Figure 6(a) shows the average mass loss rates of the as-cast and T4-treated AP65 alloys immersed in sodium chloride solution for 12 and 60 h. For both alloys, the mass loss rates increase with the increase of immersion time. The mass loss rate of the as-cast alloy is larger than that of the T4-treated one for both 12 and 60 h immersions. This means that the corrosion resistance of the as-cast AP65 alloy can be improved after T4 treatment. Besides, for the T4-treated alloy, the difference of the mass loss rate between 12 and 60 h immersions is more significant than that of the as-cast one, indicating that it is easier for the corrosion of the as-cast alloy to reach steady state than the T4-treated one. This can be verified by the hydrogen evolution volumes and rates of AP65 alloys as a function of immersion time shown in Fig. 6(b) and (c), respectively. According to Fig. 6(b), the hydrogen evolution rate of the as-cast alloy becomes linear and the corrosion comes into steady state after about 10 h immersion, which is shorter than that of the T4-treated one. According to Fig. 6(c), when the corrosions of both alloys come into steady state, the corrosion rate of the as-cast alloy based on the evolved hydrogen is 2.12 mL/cm$^2$/h, which is larger than that of the T4-treated one (0.99 mL/cm$^2$/h). This is consistent with the relationship between the mass loss rates of the two alloys. According to Fig. 4(a) and (b), almost the whole surface of the as-cast alloy is severely attacked while the severely corroded area in the T4-treated one is much smaller, which can also indicate that it is easier for the corrosion of the as-cast alloy to reach steady state than the T4-treated one. The difference between the mass loss rates and hydrogen evolution rates of the as-cast and T4-treated alloys can be ascribed to the different microstructures. In the as-cast alloy, the second phases with high free corrosion potential accelerate the microgalvanic corrosion of the surrounding lead-enriched area. Besides, the lead-enriched area in the as-cast alloy is more susceptible to be attacked. Thus, with the high activity of the lead-enriched area, the corrosion of the as-cast alloy will be accelerated during immersion tests, leading to the larger mass loss rate and hydrogen evolution rate of the as-cast alloy compared with those of the T4-treated one. In the T4-treated alloy, the alloy elements distribute homogeneously and the local corrosion is not observed. Only general corrosion exists in the T4-treated alloy. Therefore, its corrosion resistance can be improved.

### 3.4 Electrochemical Impedance Spectroscopy of AP65 Alloy

To further investigate the difference in the corrosion behavior between the as-cast and T4-treated AP65 alloys, electrochemical impedance spectroscopy (EIS) was used and the measured spectra in Nyquist plot are displayed in Fig. 7. The spectra for both alloys have a larger capacitive loop in the high frequency region and a smaller capacitive loop in the low frequency range. The difference between the spectra of the two alloys is in their capacitive loops diameters, the T4-treated alloy

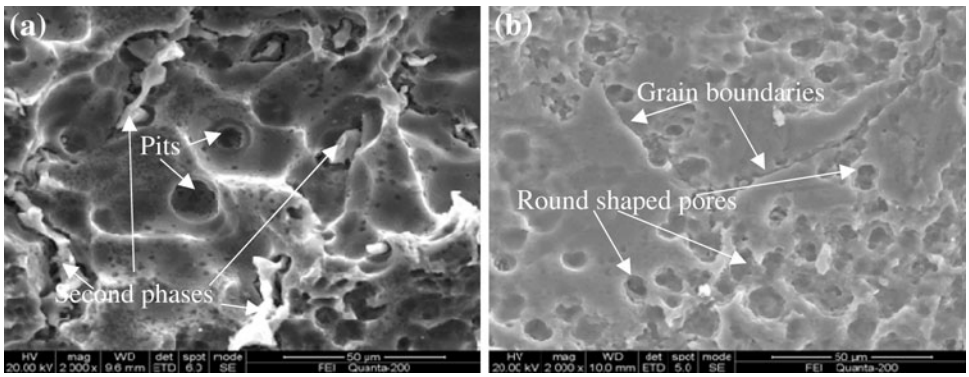


**Fig. 5** SE (secondary electron) corrosion morphologies of AP65 alloys immersed in sodium chloride solution for 60 h: (a) as-cast alloy and (b) T4-treated alloy

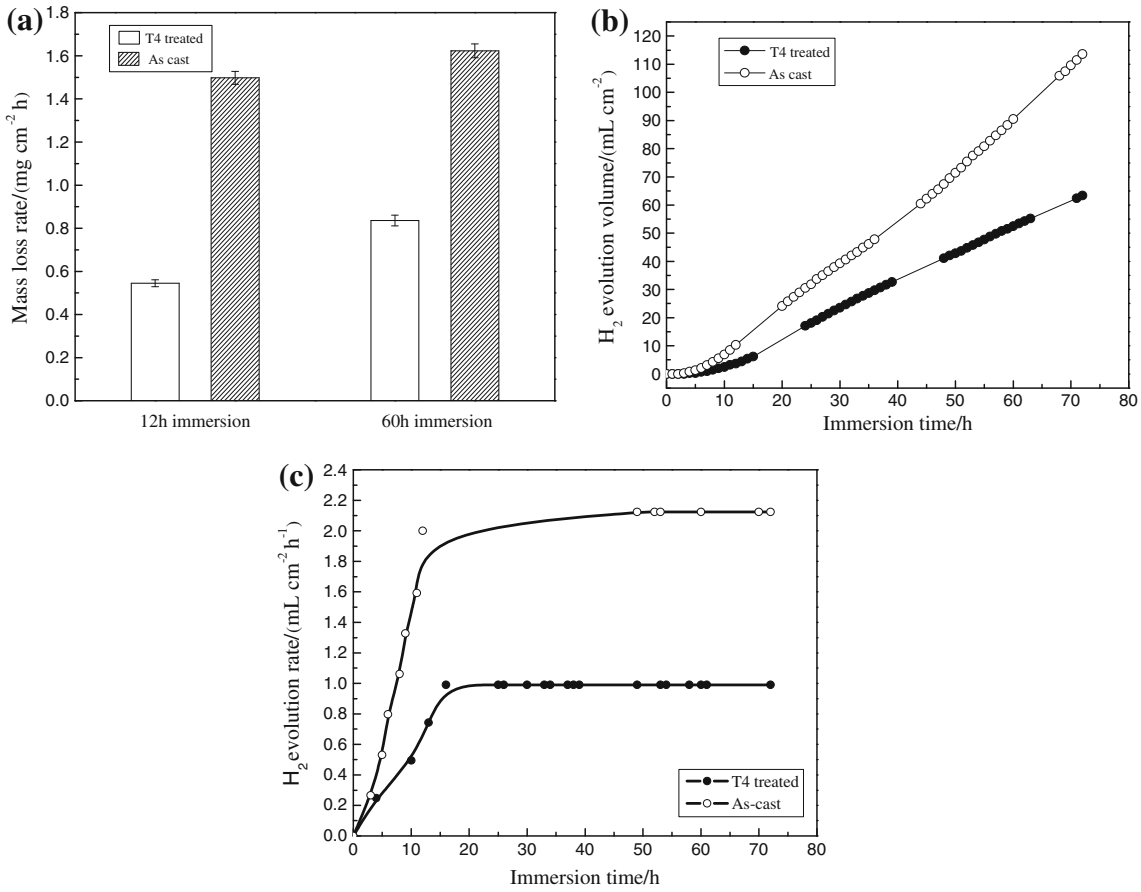


**Fig. 6** Mass loss rates for various periods of immersion (a), hydrogen evolution volumes as a function of immersion time (b), and hydrogen evolution rates as a function of immersion time (c) of AP65 alloys immersed in sodium chloride solution

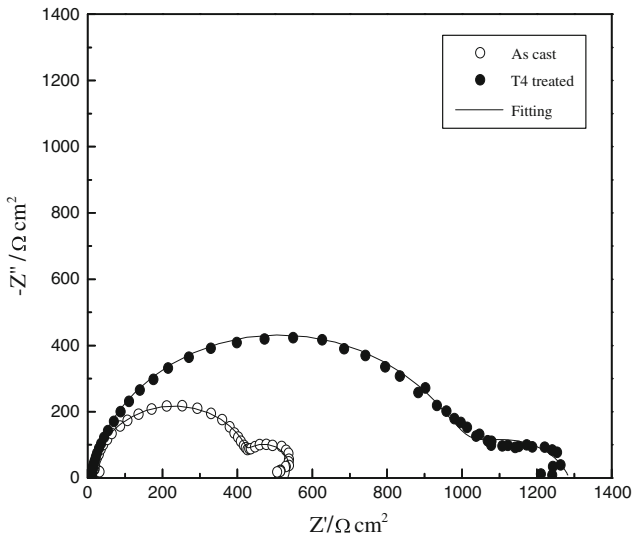


**Fig. 7** Electrochemical impedance spectra of AP65 alloys

being larger than those of the as-cast one. The capacitive loop at high frequency is equivalent to a double layer capacitance $C_{dl}$ and charge transfer resistance $R_t$, which is closely related to the potential-dependent electrochemical reactions at the interface between the electrode and solution. The capacitive loop at low frequency is related to the corrosion products, $Mg(OH)_2$ film, precipitated on the alloy surface and the relaxation of mass transport (probably $Mg^+$) in the growing $Mg(OH)_2$ film (Ref 3). The $Mg(OH)_2$ film forms by a precipitation reaction when the dissolved $Mg^{2+}$ ion concentration at the corroding surface exceeds the solubility limit (Ref 9). According to Cao (Ref 18), if the electrode reaction is controlled by one surface state variable, such as the area fraction (θ) of the alloy surface covered with $Mg(OH)_2$ film, then the Faradaic admittance $Y_F$ can be expressed as:

$$Y_F = 1/R_t + (\partial I_F/\partial\theta)(\partial\theta'/\partial E)/[j\omega - \partial\theta'/\partial\theta], \qquad \text{(Eq 1)}$$

where $R_t$ is the charge transfer resistance, $I_F$ is the Faradaic current density, θ is the area fraction of the anode surface covered with $Mg(OH)_2$ film, $E$ is the potential, ω is the excitation frequency, $j = \sqrt{-1}$, $\theta' = d\theta/dt$, and $t$ is the time.

During Faradaic electrochemical reaction process, Faradaic current density ($I_F$) decreases as the increase of the area fraction (θ) covered with $Mg(OH)_2$ film, thus $\partial I_F/\partial\theta < 0$. As the potential ($E$) increases, the concentration of $Mg^{2+}$ ions dissolving into the solution near the surface of the alloy increases, accelerating the precipitation of $Mg(OH)_2$ film on the corroded surface, therefore $\partial\theta'/\partial E > 0$. This means $(\partial I_F/\partial\theta)(\partial\theta'/\partial E) < 0$ in Eq 1 and there should be a capacitive loop at low frequency range caused by the precipitated $Mg(OH)_2$ film (Ref 9), which is consistent with Nyquist diagram shown in Fig. 7. The fitted electrochemical parameters

for EIS of both alloys are summarized in Table 2. The equivalent circuit of EIS for both alloys is shown in Fig. 8. $R_s$ is the solution resistance, $C_f$ and $R_f$ are the capacitance and resistance of the $Mg(OH)_2$ film, respectively. As the existence of dispersion effect, the capacitances of the double layer and the $Mg(OH)_2$ film are substituted by the constant phase elements $CPE_{dl}$ and $CPE_f$, respectively. According to Table 2, the charge transfer resistance ($R_t$) of the T4-treated alloy is 1005 Ω cm$^2$, which is larger than that of the as-cast one (435 Ω cm$^2$). This means the electrochemical activity of the T4-treated alloy is weaker than that of the as-cast one. The resistance caused by the $Mg(OH)_2$ film ($R_f$) of the T4-treated alloy is also larger than that of the as-cast one, indicating that it is easier for the corrosion products of the as-cast alloy to peel off from the surface of the alloy. The distance from the highest frequency to the lowest frequency on the $Z'$ coordinate in the Nyquist plot is equal to the polarization resistance of the electrode system, which can be associated with the corrosion resistance of the electrode. The larger the distance, the larger corrosion resistance the electrode will have. According to Fig. 7, the distance of the T4-treated alloy is larger than that of the as-cast one, thus the as-cast alloy has lower corrosion resistance, which is consistent with the mass loss rates and hydrogen evolution volumes (Fig. 6). The stronger electrochemical activity and the lower corrosion resistance of the as-cast alloy can be ascribed to the lead-enriched areas surrounding the second phases. According to the corrosion morphologies shown in Fig. 3, the lead-enriched areas are susceptible to be attacked, thus they have high activity and can act as places for preferential anodic dissolution, leading to the stronger electrochemical activity and lower corrosion resistance of the as-cast alloy compared with those of the T4-treated one.

### 3.5 Potentiodynamic Polarization Curves of AP65 Alloy

The polarization curves shown in Fig. 9 can exhibit a steady electrochemical process over a wide potential range, which is helpful in the understanding of the corrosion behavior of the as-cast and T4-treated AP65 alloys. According to Fig. 9, the cathodic polarization branches of the as-cast and T4-treated alloys overlap together, indicating that both alloys have similar cathodic hydrogen evolution behavior. The corrosion potential of the as-cast alloy is −1.57 V vs SCE, which is more negative than that of the T4-treated one (−1.52 V vs SCE). At the same anodic potential, the anodic polarization current density of the as-cast alloy is larger than that of the T4-treated one. This means that the as-cast alloy has larger anodic dissolution rate compared with the T4-treated one. Besides, the polarization curves are not typical. They cannot be described by a Tafel equation. The linear regions on the anodic and cathodic curves after extrapolation do not intersect at their corrosion potentials. According to Song (Ref 19), the anodic hydrogen evolution is the main cause of this phenomenon. If we ignore the anodic Tafel regions and estimate the corrosion rates by extrapolating the cathodic Tafel regions back to their corrosion potentials, we can see that the corrosion current density of the as-cast alloy is 0.065 mA/cm$^2$, which is larger than that of the T4-treated one (0.04 mA/cm$^2$). This is consistent with the mass loss rates and polarization resistances of the alloys. The cathodic potential value used here for extrapolating the cathodic Tafel region is 300 mV more negative than the corrosion potential as the cathodic branch is linear around this potential.

To compare and illustrate the difference in polarization curves between the as-cast and T4-treated alloys, a simplified polarization curve diagram is provided in Fig. 10. According to Song (Ref 19), a polarization curve measured in experiment is an apparent one. The anodic and cathodic currents are the sum of real anodic and cathodic currents at given polarization potentials. Only when the polarization potential has significantly shifted away from the corrosion potential and the real anodic or cathodic current become negligible, can the apparent cathodic or anodic current be equal to the real cathodic or anodic one. In Fig. 10, $I_a^s$, $I_c^s$, $I_a^c$, and $I_c^c$ are real anodic and cathodic current densities of the T4-treated and as-cast alloys, respectively. They are plotted like those in Fig. 10 according to

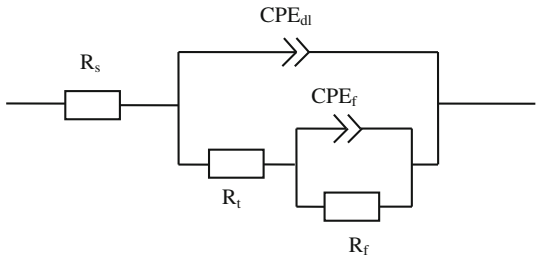


**Fig. 8** Equivalent circuits for EIS of T4-treated and as-cast AP65 alloys

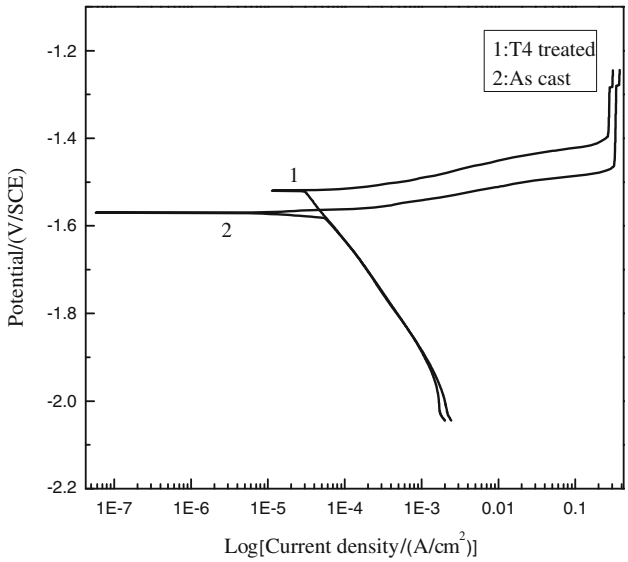


**Fig. 9** Potentiodynamic polarization curves of AP65 alloys

**Table 2 Electrochemical parameters obtained by fitting analysis of EIS of T4-treated and as-cast AP65 alloys**

| Alloy | $R_s$, Ω cm$^2$ | $CPE_{dl}$-T, F/cm$^2$ | $CPE_{dl}$-P | $R_t$, Ω cm$^2$ | $CPE_f$-T, F/cm$^2$ | $CPE_f$-P | $R_f$, Ω cm$^2$ |
|---|---|---|---|---|---|---|---|
| T4 treated | 5 | $2 \times 10^{-5}$ | 0.9 | 1005 | $5 \times 10^{-3}$ | 0.77 | 274 |
| As-cast | 15 | $1.1 \times 10^{-5}$ | 1 | 435 | $4 \times 10^{-4}$ | 1.3 | 85 |

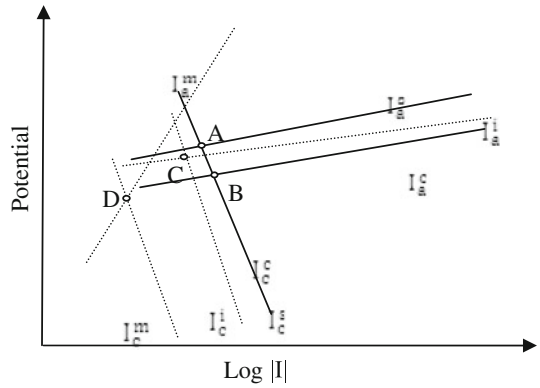


**Fig. 10** Schematic illustration of real polarization curves of as-cast and T4-treated AP65 alloys. $I_a^s$, $I_c^s$, $I_a^c$, and $I_c^c$ are real anodic and cathodic current densities of T4-treated and as-cast alloys, respectively. $I_a^i$ and $I_c^i$ are real anodic and cathodic current densities of second phases in as-cast alloy, respectively. $I_a^m$ and $I_c^m$ are real anodic and cathodic current densities of α-Mg matrix in as-cast alloy, respectively

the experimental polarization curves shown in Fig. 9. In Fig. 10, $I_c^s$ and $I_c^c$ overlap together and $I_a^c$ is larger than $I_a^s$ at the same anodic potential. Besides, point B, corresponding to the corrosion potential of the as-cast alloy, is lower than point A related to the corrosion potential of the T4-treated one. These are consistent with the experimental curves (Fig. 9). In order to explain the experimental phenomenon shown in Fig. 9, $I_a^c$ and $I_c^c$ are needed to be further decomposed for analysis.

According to Fig. 1(a), the as-cast alloy consists of the second phase, lead-enriched area and α-Mg matrix. Thus, it can be decomposed into two parts: the α-Mg matrix and the second phase plus the lead-enriched area. The α-Mg matrix of the as-cast alloy should have the same microstructure as that of the lead-enriched area except its content of lead is low. The second phases are surrounded by the lead-enriched areas, which have different chemical composition and electrochemical activity from those of the α-Mg matrix. Therefore, in this study, the lead-enriched areas are particularly classified into the second phases. Their contribution to the second phases will be mainly the anodic behavior, as the second phases are normally relatively inert in anodic dissolution. The schematic presentations of the second phase plus the lead-enriched area are shown in Fig. 11(a). Lead has low exchange current density of hydrogen evolution and the cathodic hydrogen reaction is relatively difficult on its surface (Ref 18). Hence, the real cathodic current density $I_c^i$ for the second phase surrounded by the lead-enriched area in the as-cast alloy is lower than that for the T4-treated alloy ( $I_c^s$) (see Fig. 10). In the as-cast alloy, the cathodic polarization current density of the β-phase is higher than that of the α-Mg matrix (Ref 20). Therefore, the real cathodic current densities $I_c^m$ and $I_c^i$ for the α-Mg matrix and second phase, respectively, are plotted as those in Fig. 10. According to Fig. 3(a) and (b), the lead-enriched area surrounding the second phase is susceptible to be attacked during immersion test. Thus, it might be active and can act as defect sites for preferential anodic dissolution, leading to the peeling off of the second phase for long time immersion (see Fig. 11b, c). Therefore, the real anodic current density $I_a^i$ for the second phase surrounded by the lead-enriched area is higher than $I_a^s$ for the T4-treated alloy and $I_a^m$ for the α-Mg matrix in the as-cast alloy as plotted in Fig. 10. For the as-cast alloy, the α-Mg

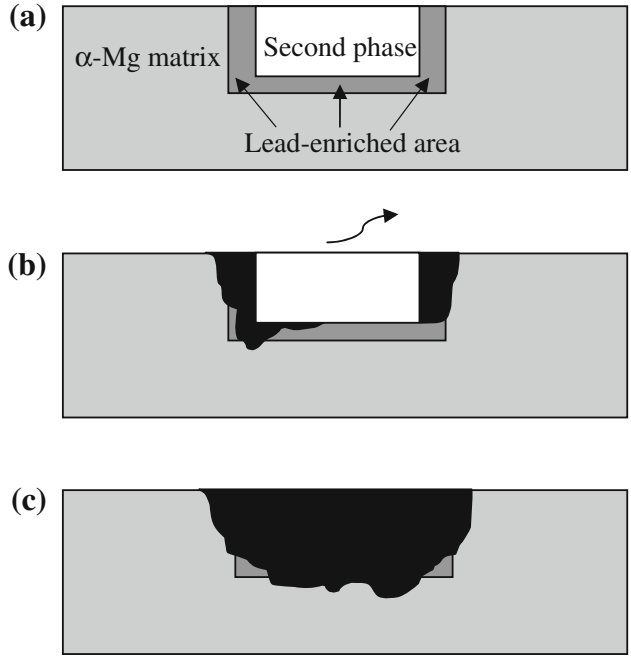


**Fig. 11** Schematic presentations of (a) second phase plus lead-enriched area in as-cast AP65 alloy, (b) dissolution of lead-enriched area surrounding second phase, and (c) peeling off of second phase as a result of preferential dissolution of lead-enriched area

matrix with less contents of alloying elements suffers less attack (see Fig. 3) and its anodic dissolution rate should be lower than that of the second phases. Thus, the slope of $I_a^m$ should be larger than those of others (see Fig. 10), which is consistent with what Song had reported about AM70 alloy added with tin (Ref 19). The contributions of $I_c^i$ and $I_c^m$ to $I_c^c$ make $I_c^c$ close to $I_c^s$. The influence of $I_a^i$ on $I_a^c$ is significant, which can make $I_a^c$ larger than $I_a^s$ at the same anodic potential. This might be the reason why the cathodic polarization branches of the as-cast and T4-treated alloys overlap together and the anodic polarization current density of the as-cast alloy is larger than that of the T4-treated one at the same anodic potential. Points C and D are related to the corrosion potential of the second phase and the α-Mg matrix in the as-cast alloy, respectively. Both of them are more negative than that of the T4-treated one (point A). The corrosion potential of the as-cast alloy should be located between points C and D. Therefore, it is more negative than the corrosion potential of the T4-treated alloy.

It should be stressed that the real anodic and cathodic current densities cannot be measured easily. The real polarization curves in Fig. 10 are plotted according to the experimental (apparent) ones in Fig. 9. The assumptions made in Fig. 10 can be supported by the corrosion morphologies shown in Fig. 3-5. Therefore, it is expect that the lead-enriched areas are active and can act as the places for preferential anodic dissolution, leading to the peeling off of the second phases after long time immersion.

## 4. Conclusion

The corrosion behavior of the as-cast and T4-treated magnesium alloy AP65 in 3.5% sodium chloride solution was

investigated. In the as-cast AP65 alloy, the second phases $Mg_{17}Al_{12}$ surrounded by the lead-enriched areas distribute discontinuously along the grain boundaries. The lead-enriched areas with high activity are susceptible to be attacked during immersion test and can act as the places for preferential anodic dissolution, leading to the lower charge transfer resistance and larger anodic polarization current density of the as-cast alloy compared with those of the T4-treated one. As the immersion time increases, the lead-enriched areas dissolve into sodium chloride solution, leading to the peeling off of the second phases and the disappearance of the round-shaped pores distributing on the lead-enriched areas. After T4 treatment, the second phases and the lead-enriched areas dissolve into the magnesium matrix and the corrosion resistance can be improved. The T4-treated AP65 alloy suffers general corrosion that initiates in the form of round-shaped pores distributing homogeneously within the grain and along the grain boundaries.

## References


1. R. Renuka, Influence of Allotropic Modifications of Sulfur on the Cell Voltage in Mg-CuI(S) Seawater Activated Batter, *Mater. Chem. Phys.*, 1999, **59**(42), p 42–48
2. Y. Feng, R.C. Wang, K. Yu, C.Q. Peng, and W.X. Li, Influence of Ga and Hg on Microstructure and Electrochemical Corrosion Behavior of Mg Alloy Anode Materials, *Trans. Nonferrous Met. Soc. China*, 2007, **17**, p 1363–1366
3. D.X. Cao, L. Wu, G.L. Wang, and Y.Z. Lu, Electrochemical Oxidation Behavior of Mg-Li-Al-Ce-Zn and Mg-Li-Al-Ce-Zn-Mn in Sodium Chloride Solution, *J. Power Sources*, 2008, **183**(800), p 799–804
4. Y. Feng, R.C. Wang, C.Q. Peng, and N.G. Wang, Influence of $Mg_{21}Ga_5Hg_3$ Compound on Electrochemical Properties of Mg-5%Hg-5%Ga Alloy, *Trans. Nonferrous Met. Soc. China*, 2009, **19**(155), p 154–159
5. R.K. Venkatesara, Performance Evaluation of Mg-AgCl Batteries for Under Water Propulsion, *Def. Sci. J.*, 2001, **5**(2), p 165–170
6. M.C. Zhao, P. Schmutz, S. Brunner, M. Liu, G.L. Song, and A. Atrens, Influence of pH and Chloride Ion Concentration on the Corrosion of Mg Alloy ZE41, *Corros. Sci.*, 2008, **50**, p 3168–3178
7. Z.M. Shi, G.L. Song, and A. Atrens, Corrosion Resistance of Anodised Single-Phase Mg Alloys, *Corros. Sci.*, 2005, **201**, p 492–503
8. M.C. Zhao, P. Schmutz, S. Brunner, M. Liu, G.L. Song, and A. Atrens, An Exploratory Study of the Corrosion of Mg Alloys During Interrupted Salt Spray Testing, *Corros. Sci.*, 2009, **51**, p 1277–1292
9. M.C. Zhao, M. Liu, G.L. Song, and A. Atrens, Influence of the β-Phase Morphology on the Corrosion of the Mg Alloy AZ91, *Corros. Sci.*, 2008, **50**, p 1939–1953
10. X.N. Gu, Y.F. Zheng, Y. Cheng, S.P. Zhong, and T.F. Xi, In Vitro Corrosion and Biocompatibility of Binary Magnesium Alloys, *Biomaterials*, 2009, **30**, p 484–498
11. A. Pardo, M.C. Merion, A.E. Coy, F. Viejo, R. Arrabal, and S. Feliujr, Influence of Microstructure and Composition on the Corrosion Behavior of Mg/Al Alloys in Chloride Media, *Electrochim. Acta*, 2008, **53**, p 7890–7902
12. S. Candan, M. Unal, M. Turkmen, E. Koc, Y. Turen, and E. Candan, Improvement of Mechanical and Corrosion Properties of Magnesium Alloy by Lead Addition, *Mater. Sci. Eng. A*, 2009, **501**, p 115–118
13. A.D. Sudholz, N. Birbilis, C.J. Bettles, and M.A. Gibson, Corrosion Behavior of Mg-Alloy AZ91E With Atypical Alloying Additions, *J. Alloys Compd.*, 2009, **471**, p 109–115
14. R. Udhayan and D.P. Bhatt, On the Corrosion Behavior of Magnesium and Its Alloys Using Electrochemical Techniques, *J. Power Sources*, 1996, **63**, p 103–107
15. A. Srinivasan, U.T.S. Pillai, and B.C. Pai, Effect of Pb Addition on Ageing Behavior of AZ91 Magnesium Alloy, *Mater. Sci. Eng. A*, 2007, **452-453**, p 87–92
16. G.L. Song, A. Atrens, and M. Dargusch, Influence of Microstructure on the Corrosion of Diecast AZ91D, *Corros. Sci.*, 1999, **41**, p 249–273
17. L.M. Petrova and V.V. Krasnoyarakii, Anodic Behavior of Magnesium-Lead Binary Alloys in Neutral Solutions, *Zashch. Met.*, 1988, **24**, p 277–280
18. C.N. Cao, *Principles of Electrochemistry of Corrosion*, 3rd ed., Chemical Industry Press, Beijing, 2008
19. G.L. Song, Effect of Tin Modification on Corrosion of AM70 Magnesium Alloy, *Corros. Sci.*, 2009, **51**, p 2163–2170
20. Z.M. Shi, M. Liu, and A. Atrens, Measurement of the Corrosion Rate of Magnesium Alloys Using Tafel Extrapolation, *Corros. Sci.*, 2010, **52**, p 579–588